CHEMISTRY OF MATERIALS

Downloaded via BUTLER UNIV on May 15, 2021 at 05:04:24 (UTC).
See https://pubs.acs.org/sharingguidelines for options on how to legitimately share published articles.

Order and Disorder: Toward the Thermodynamically Stable α-$BaMoO_2F_4$ from the Metastable Polymorph

Hongil Jo, Min Hyung Lee, and Kang Min Ok*

Cite This: Chem. Mater. 2021, 33, 1875−1882

Read Online

ACCESS | Metrics & More | Article Recommendations | SI Supporting Information

ABSTRACT: A fully ordered noncentrosymmetric barium molybdenum oxyfluoride, α-$BaMoO_2F_4$, has been synthesized by a hydrothermal reaction at 200 °C in a concentrated hydrofluoric acid solution. A centrosymmetric polymorph with O/F disorder, β-$BaMoO_2F_4$, has been obtained in several minutes when the reaction mixture was stirred at room temperature in the same medium. Interestingly, we found that the metastable β-$BaMoO_2F_4$ transforms into the thermodynamically stable α-$BaMoO_2F_4$ in an ambient condition. More detailed kinetic studies using powder X-ray diffraction indicate that the MoO_2F_4 octahedra in the kinetic phase, β-$BaMoO_2F_4$, rearrange through the constant dissolution/precipitation process to find a more stable orientation and form the fully ordered α-$BaMoO_2F_4$. Density functional theory (DFT) calculations suggest that the formation of the thermodynamically stable α-$BaMoO_2F_4$ is driven by the strong Mo−O π-interactions induced by Ba^{2+} cations. The new finding on the understanding of the kinetics of solid-state reactions suggests a novel way toward an effective discovery of functional materials with asymmetric structures.

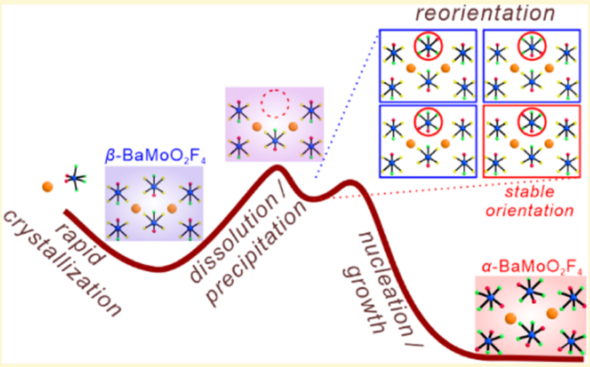

■ INTRODUCTION

Synthetic chemists have continuously combined most elements in the periodic table to discover new compounds with interesting structures and properties through carefully designed methods. In general, the majority of the isolated reaction products under normal reaction conditions often turn out to be thermodynamically stable phases. However, quite a lot of unidentified metastable phases with potentially exciting characteristics exist in local energy minima throughout the synthetic reactions. Therefore, carefully controlled reaction conditions might lead us to the discovery of exciting kinetic polymorphs with unexpected structures and properties. Several comparison studies on the reactivity and stability for a number of phase transition reactions for polymorphs have been reported to date.[1−12] However, efforts to elucidate the underlying reaction mechanisms related to symmetry have rarely been put in to design functional materials more efficiently.

Among many functional compounds, metal oxyfluorides with d^0 transition-metal cations have been of great interest because the fluorination of metal oxides can give significant structural and property variations.[13−16] Frameworks of many metal oxyfluorides are composed of a variety of distorted polyhedral units. In fact, combining the asymmetric units during the synthesis would be highly advantageous toward the crystallization of macroscopic noncentrosymmetric (NCS) structures that may exhibit excellent nonlinear optical (NLO) properties in a wide energy range.[17−27] Especially, the second-order Jahn−Teller (SOJT) distortive cation, Mo^{6+}, has been identified as one of the strongest distorters.[28,29] Thus, molybdenum oxyfluorides have been expected to exhibit diverse asymmetric structural features.[30,31] A few representative molybdenum oxyfluorides include peculiar helical chains containing periodical tendril perversion [$A_2MoO_2F_3$ (A = Rb, NH_4, and Tl)],[32] perovskites exhibiting unique features of atomic ordering and octahedral tilting [$Na_2MoO_2F_4$ and α-$A_3MoO_3F_3$ (A = K and Rb)],[33,34] luminescence materials with high thermal stability [$CsMoO_2F_3$, K_3MoOF_7, and $K_2MoO_2F_4 \cdot H_2O$],[35−37] and large birefringence materials [$K_6Mo_4O_8F_{10}$ and $Na_3Cs(MoO_2F_4)_2$].[38,39] It should be noted that most of the reported molybdenum oxyfluorides include monovalent cations. Here, we introduced divalent cations to a metal oxyfluoride system to more effectively control the symmetry of crystal structures. Specifically, we wanted to study the effect of larger Coulombic interactions between divalent cations and oxides/fluorides on the alignment of MoO_xF_{6-x} units as well as macroscopic centricity. By doing so, we were able to synthesize three isostructural NCS compounds, $SrMoO_2F_4$, α-$BaMoO_2F_4$, and $PbMoO_2F_4$, and one centrosymmetric (CS) compound, β-$BaMoO_2F_4$. Interestingly, we found that β-$BaMoO_2F_4$ can be

Received: January 8, 2021
Revised: February 14, 2021
Published: February 25, 2021

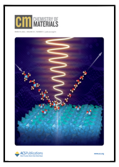

ACS Publications
© 2021 American Chemical Society

https://dx.doi.org/10.1021/acs.chemmater.1c00074

transformed into α-$BaMoO_2F_4$ under mild reaction conditions. In this paper, we propose a plausible mechanism for the phase transformation reaction through detailed kinetic analyses using lab-source powder X-ray diffraction (PXRD). Furthermore, the driving force of the formation of α-$BaMoO_2F_4$ is discussed using the crystal structure analysis and density functional theory (DFT) calculations. We believe that the new findings on the formation of more stable α-$BaMoO_2F_4$ and elucidating a detailed mechanism for the solid-state reaction should suggest a new direction toward the discovery of materials with asymmetric structures more systematically.

■ RESULTS AND DISCUSSION

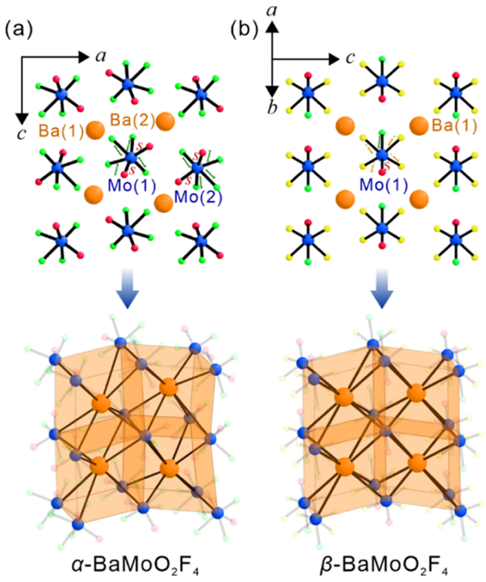

Figure 1. Ball-and-stick model of (a) α-$BaMoO_2F_4$ and (b) β-$BaMoO_2F_4$ (orange, Ba; blue, Mo; red, O; green, F; yellow, O/F). While the MoO_2F_4 octahedra in fully ordered α-$BaMoO_2F_4$ exhibit two short Mo−O and four long Mo−F bonds, those in disordered β-$BaMoO_2F_4$ exhibit, along a corner, one short Mo−O bond, four intermediate Mo−O/F bonds, and one long Mo−F bond (local C_4 direction). *s*, *l*, and *i* represent short, long, and intermediate, respectively. If $MoO_2F_4^{2-}$ octahedra are assumed to be huge anions, the structures of both α-$BaMoO_2F_4$ and β-$BaMoO_2F_4$ can be considered as a distorted CsCl-type structure.

Pure colorless crystals of α-$BaMoO_2F_4$ have been grown via a hydrothermal reaction in 62% yield using $BaMoO_4$ and HF solution at 200 °C for 72 h. α-$BaMoO_2F_4$ crystallizes in a polar orthorhombic space group, *Pca*2_1 (no. 29), and features a molecular structure that is composed of two crystallographically independent Ba^{2+} cations and $MoO_2F_4^{2-}$ octahedra (Figure 1a and Table S1). Because all oxides and fluorides in $MoO_2F_4^{2-}$ octahedra are fully ordered, two short Mo−O bonds [1.673(13)−1.781(11) Å] and four long Mo−F bonds [1.864(9)−2.113(9) Å] are clearly observed. If we assume a $MoO_2F_4^{2-}$ octahedron as a huge single anion, the structure of α-$BaMoO_2F_4$ can be considered as a distorted CsCl-type structure, in which the Ba^{2+} cation is surrounded by eight $MoO_2F_4^{2-}$ in corners of a cube (Figure 1a). Ba^{2+} cations interact with F^- and O^{2-} anions with Ba−F and Ba−O contact distances of 2.589(8)−2.971(11) and 2.772(12)−3.280(13) Å, respectively (Table S3). Interestingly, it should be noted that Ba−F distances are shorter than those of Ba−O. Besides, Ba^{2+} cations prefer to interact with F^- anions rather than O^{2-} anions: while both Ba(1) and Ba(2) interact with seven F^- anions, only three and two O^{2-} anions contact with $Ba(1)^{2+}$ and $Ba(2)^{2+}$ cations, respectively. Thus, the distorted MoO_2F_4 octahedra are arranged in a tilted manner to optimize the Ba−F and Ba−O interactions. Bond valence sum calculations on α-$BaMoO_2F_4$ result in values of 2.12−2.20, 5.74−6.00, 1.66−2.02, and 0.98−1.08 for Ba, Mo, O, and F, respectively.[40] To compare a variety of physicochemical properties, crystals of two other isostructural divalent metal molybdenum oxyfluorides, $SrMoO_2F_4$ and $PbMoO_2F_4$, have also been grown through similar hydrothermal reactions (Supporting Information).

A stoichiometrically equivalent metastable polymorph, β-$BaMoO_2F_4$, has also been prepared by adding BaF_2 to a solution of MoO_3−HF. Once the reaction mixture was thoroughly stirred, pure polycrystalline samples of β-$BaMoO_2F_4$ were synthesized in 76% yield in 5 min at room temperature. The crystal structure determined using PXRD indicates that β-$BaMoO_2F_4$ crystallizing in the centrosymmetric space group, *Cmcm*, exhibits a molecular structure composed of Ba^{2+} cations and $MoO_2F_4^{2-}$ octahedra. The cationic distortion of MoO_2F_4 octahedra containing the O/F disorder in β-$BaMoO_2F_4$, however, occurs along a corner (local C_4 direction), which results in one short Mo−O [1.696(10) Å] bond, four intermediate Mo−O/F [1.876(4) Å] bonds, and one long Mo−F [2.187(7) Å] bond (Figure 1b). It should be noted that the O(2)/F(2) positions are statistically disordered with a 0.25/0.75 ratio, which might occur because of the fast crystallization time. Attributable to the O/F disorder, the preferred Ba−F interactions over Ba−O interactions found in α-$BaMoO_2F_4$ are not observed in β-$BaMoO_2F_4$. More importantly, the parallel array of Ba^{2+} cations along the *c*-axis originating from the lack of the favorable Ba−F interactions have β-$BaMoO_2F_4$ to crystallize in the *CS* space group. Bond valence sum calculations on β-$BaMoO_2F_4$ result in values of 2.12, 5.70, 1.87, 1.25, and 1.04 for Ba^{2+}, Mo^{6+}, O^{2-}, (O^{2-}/F^-), and F^-, respectively.[40]

The infrared (IR) spectra of the reported compounds reveal Mo−O and Mo−F vibrations at ca. 966−897 and 579−400 cm^{-1}, respectively (Figure S6).[39,41−43] Although the IR spectra of α- and β-$BaMoO_2F_4$ are very similar, two bands occurring at ca. 500−600 cm^{-1} due to Mo−F vibrations of α-$BaMoO_2F_4$ merged to form a broad single band for β-$BaMoO_2F_4$ attributable to the O/F disorder. Band gaps of $SrMoO_2F_4$, α-$BaMoO_2F_4$, β-$BaMoO_2F_4$, and $PbMoO_2F_4$ are estimated to be ca. 3.42, 3.30, 3.40, and 3.20 eV, respectively, and the values are obtained by converting wavelengths in the ultraviolet−visible (UV−vis) diffuse reflectance spectra using the Kubelka−Munk function (Figure S7).[44] The band gaps of the isostructural compounds decrease as the polarizability of valence electrons in divalent cations increases. Structures of $SrMoO_2F_4$, α-$BaMoO_2F_4$, β-$BaMoO_2F_4$, and $PbMoO_2F_4$ are thermally stable at ca. 430, 310, 300, and 380 °C, respectively. Upon further heating, the materials thermally decompose to the corresponding divalent metal molybdenum oxides and (oxy)fluorides (Figures S8 and S9).

Powder second-harmonic generation (SHG) measurements on the graded polycrystalline samples indicate that $SrMoO_2F_4$, α-$BaMoO_2F_4$, and $PbMoO_2F_4$ exhibit mild SHG efficiencies 1.1, 0.7, and 0.5 times that of α-SiO_2 (45−63 μm), respectively, and phase-matching behaviors (Figure 2a). To understand the structural origin of the SHG, moments arising

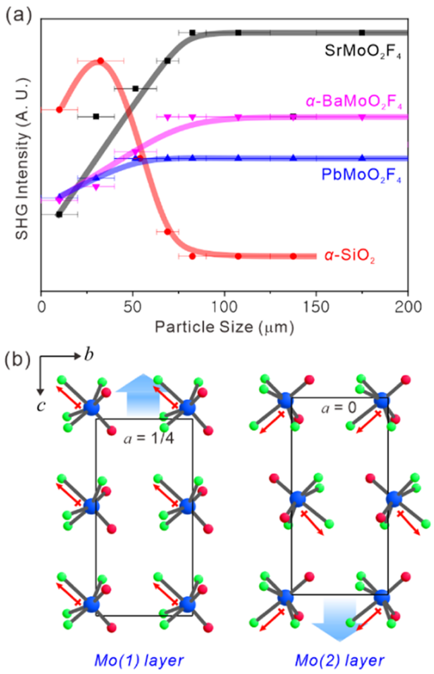

Figure 2. (a) SHG intensity versus particle size for $AMoO_2F_4$ (A = Sr, Ba, and Pb) and α-SiO_2. The curves are drawn to guide the eyes. (b) Polarizations from $Mo(1)O_2F_4$ octahedra point toward the approximate $[10\bar{1}]$ and $[\bar{1}0\bar{1}]$ directions, and moments from $Mo(2)O_2F_4$ units direct to the approximate $[101]$ and $[\bar{1}01]$ directions. Thus, a weak net moment occurs along the $[\bar{1}00]$ direction attributed to the different degree of MoO_2F_4 octahedral distortions.

from the distorted MoO_2F_4 octahedra in α-$BaMoO_2F_4$ were analyzed. As seen in Figure 2b, while polarizations from $Mo(1)O_2F_4$ octahedra point toward the approximate $[10\bar{1}]$ and $[\bar{1}0\bar{1}]$ directions, moments from $Mo(2)O_2F_4$ units direct to the approximate $[101]$ and $[\bar{1}01]$ directions. Although a net moment occurs along the $[\bar{1}00]$ direction attributed to the different degree of MoO_2F_4 octahedral distortions, the antiparallel alignment of $Mo(1)O_2F_4$ and $Mo(2)O_2F_4$ octahedra is responsible for the mild SHG for the reported compounds. Local dipole moment calculations suggest that the dipole moments of distortive MoO_2F_4 octahedra range from 4.8 to 5.7 D (Table S7).

Crystals of $SrMoO_2F_4$ and α-$BaMoO_2F_4$ turn out to emit yellow and orange luminescence, respectively, upon irradiation with a UV lamp (Figure S10a). Photoluminescence (PL) spectra measured under 350 nm radiations indicate that $SrMoO_2F_4$ and α-$BaMoO_2F_4$ exhibit broad emissions with a full width at half-maximum of ca. 100 nm centered at 594 and 610 nm, respectively (Figure S10b). The PL excitation and emission bands could be assigned to LMCT and MLCT, respectively, because no d electron is available in Mo^{6+} cations from the reported compounds. PL decay curves fitted based on the third-order exponential equation[45,46] reveal that the calculated average lifetimes (τ_{avg}) for $SrMoO_2F_4$ and α-$BaMoO_2F_4$ are 544 and 336 μs, respectively (Figure S10c). Similar to those of the previously reported materials with WO_2F_4 octahedra,[47,48] the observed luminescence on $SrMoO_2F_4$ and α-$BaMoO_2F_4$ might be attributed to the distorted MoO_2F_4 octahedra stabilizing the self-trapped exciton energy level by generating polarization. The PLQYs for $SrMoO_2F_4$ and α-$BaMoO_2F_4$ are measured to be ca. 2 and 5%, respectively.

To better understand electronic structures and optical properties of the title compounds, density functional theory (DFT) calculations were performed. The calculated band gaps for $SrMoO_2F_4$, α-$BaMoO_2F_4$, β-$BaMoO_2F_4$, and $PbMoO_2F_4$ are 3.53, 3.46, 3.51, and 3.50 eV, respectively (Figure S11); the values are slightly overestimated because the spin−orbit couplings have not been considered during the DFT calculations.[49−51] While the valence band maximum (VBM) mostly consists of 2p orbitals of O and F, the conduction band minimum (CBM) is mainly composed of 4d orbitals of Mo and 2p orbitals of O and F (Figure S12). Therefore, band edges mainly comprise MoO_2F_4 units. For $PbMoO_2F_4$, however, Pb 2p orbitals make a nonnegligible contribution to the CBM attributable to the larger electron density. DFT calculations also support that MoO_2F_4 octahedra are responsible for the observed SHG properties in the reported compounds.

Thus far, a variety of metal oxyfluorides have been synthesized under mild reaction conditions.[47,52,53] Thus, an optimal synthesis condition for α-$BaMoO_2F_4$ at room temperature has been further investigated. Various synthetic attempts by mixing the MoO_3−HF solution and BaF_2 suspension at room temperature always resulted in the formation of polycrystalline β-$BaMoO_2F_4$ in 5 min, which was identified by PXRD. Surprisingly, however, we found that β-$BaMoO_2F_4$ transforms into α-$BaMoO_2F_4$ if the reaction time increases to 180 min in the HF solution at room temperature (Figure 3a). As seen in Figure 3a, while the (200), (020), and (212) peaks for β-$BaMoO_2F_4$ decrease, the (012), (410), (212), and (203) peaks for α-$BaMoO_2F_4$ increase in the reaction medium. Therefore, a more detailed kinetic study on the transformation reaction from β-$BaMoO_2F_4$ to α-$BaMoO_2F_4$ has been performed using PXRD. The extent of reaction over time has been analyzed by monitoring the change of mol % of β-$BaMoO_2F_4$ through the whole pattern-matching method. As seen in Figure 3b, the phase transformation is well-fitted to the Avrami equation.[54,55] To better understand the phase change, reactions between β-$BaMoO_2F_4$ and HF solution at different temperatures have been further investigated. The quantitative kinetic data obtained at different temperatures are also well-fitted to the Avrami expression (Figure 4a,b and Table S3).

An exponent value (n) for the Avrami equation of ca. 4 suggests that the phase transformation reaction occurs three-dimensionally. The activation energy (E_A) obtained from the Arrhenius equation is estimated to be 152 kJ/mol (Figure S13a). Using the Eyring equation,[56] the activation enthalpy ($\Delta H^{\ddagger}$) and entropy ($\Delta S^{\ddagger}$) are also calculated to be 149 kJ/mol and 143 J/(mol K), respectively (Figure S13b). The positive value of $\Delta S^{\ddagger}$ indicates that the rate-determining step for the phase change reaction is the dissolution step. Because the yield of β-$BaMoO_2F_4$ is 76%, about 24% of Ba^{2+} and $MoO_2F_4^{\,2-}$ are thought to be dissolved in the solvent. Thus, the proposed transformation mechanism can be described in the following three steps (Figure 5). First, a rapid crystallization leads the MoO_2F_4 octahedra to locate in thermodynamically unstable positions and to crystallize in β-$BaMoO_2F_4$ with the O/F disorder. Second, the reversible reaction of dissolution/precipitation makes the MoO_2F_4 units find thermodynamically more stable positions and orientations, which results in the formation of fully ordered α-$BaMoO_2F_4$ crystal seeds. Third, the newly formed nuclei of α-$BaMoO_2F_4$ crystals further

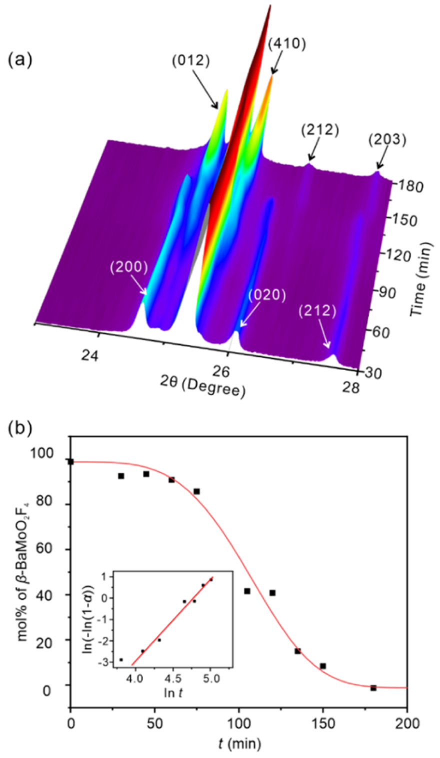

Figure 3. (a) Three-dimensional stack plot of XRD data collected for the change of β-BaMoO$_2$F$_4$ to α-BaMoO$_2$F$_4$ in the HF solution at room temperature. While the (200), (020), and (212) peaks for β-BaMoO$_2$F$_4$ decrease, the (012), (410), (212), and (203) peaks for α-BaMoO$_2$F$_4$ occur in the reaction medium. (b) Extent of reaction over time analyzed by monitoring the change of mol % of β-BaMoO$_2$F$_4$ through the whole pattern-matching method is well-fitted by the Avrami equation (red line). The inset shows the Sharp−Hancock plot for the reaction.

provide thermodynamically more stable positions, and the proportion of α-BaMoO$_2$F$_4$ increases over time.

A question remains why the CS β-BaMoO$_2$F$_4$ with the O/F disorder changes to NCS polar α-BaMoO$_2$F$_4$ under such a mild condition? In fact, β-BaMoO$_2$F$_4$ does not simply transform into α-BaMoO$_2$F$_4$ upon heating in the solid state. To understand the chemical stability, the phase transition temperature of β-BaMoO$_2$F$_4$ to α-BaMoO$_2$F$_4$ has been calculated. While the enthalpy change (ΔH) can be obtained from the DFT calculations, the entropy change (ΔS) may be estimated from the Boltzmann equation.[57−59] Since β-BaMoO$_2$F$_4$ has a disordered structure, the total energy of β-BaMoO$_2$F$_4$ has been averaged across 28 possible configurations in the unit cell. Using the relation $\Delta H = \Delta E - P\Delta V$, ΔH is calculated to be −10.14 kJ/mol.

Because α-BaMoO$_2$F$_4$ and β-BaMoO$_2$F$_4$ are stoichiometrically equivalent, the configurational entropy may make a major contribution to the entropy change. Substituting the number of configurations, namely, 1 for α-BaMoO$_2$F$_4$ and $4N_A$ (N_A = Avogadro's number) for β-BaMoO$_2$F$_4$, into the Boltzmann equation, ΔS is estimated to be −11.53 J/(mol K). Considering that the Gibbs free energy does not change at the phase transition temperature ($\Delta G = \Delta H - T\Delta S = 0$), the phase transition temperature is calculated to be 606 °C, which is much higher than the material's decomposition temperature. Therefore, α-BaMoO$_2$F$_4$ should be an enthalpy-driven thermodynamically stable phase. To confirm this, it would be necessary to explain why the oxides and fluorides in MoO$_2$F$_4$$^{2-}$ octahedra are ordered in α-BaMoO$_2$F$_4$ because the O/F ordering is uncommon in solid-state materials owing to their similar ionic radii and chemical properties. As mentioned previously, the larger Coulombic interactions between divalent cations and oxides/fluorides would affect the alignment of MoO$_2$F$_4$$^{2-}$ octahedra. Because of the off-centering distortions caused by strong π-interactions between Mo−O (primary distortion) bonds, the negative charges of anions differ from the formal charges. Thus, the distribution of negative charges was estimated from the bond valence method (Table S9).[60] The partial charges in MoO$_2$F$_4$$^{2-}$ for α-BaMoO$_2$F$_4$ are estimated to be 0.11−0.59 for oxides, 0.14−0.38 for fluorides at the *cis*-position to oxides, and 0.45−0.56 for fluorides at the *trans*-position to oxides. Thus, the two *cis*-F atoms at the *trans*-position to oxides are more negatively charged, which makes the MoO$_2$F$_4$$^{2-}$ unit preferentially interact with Ba^{2+} in the *cis*-direction. If *cis*-fluorides at the trans-position of oxides are fixed, the rotational freedom should be removed, and the O/F ordering is achieved in α-BaMoO$_2$F$_4$. Most of the O/F ordering is also achieved by hydrogen bonds.[61,62] Even a monovalent metal cation with a radius similar to that of Ba^{2+} cannot lead to the O/F disorder.[63−65] Thus, the stronger Coulomb interactions by the higher charged divalent cations should cause the O/F ordering.

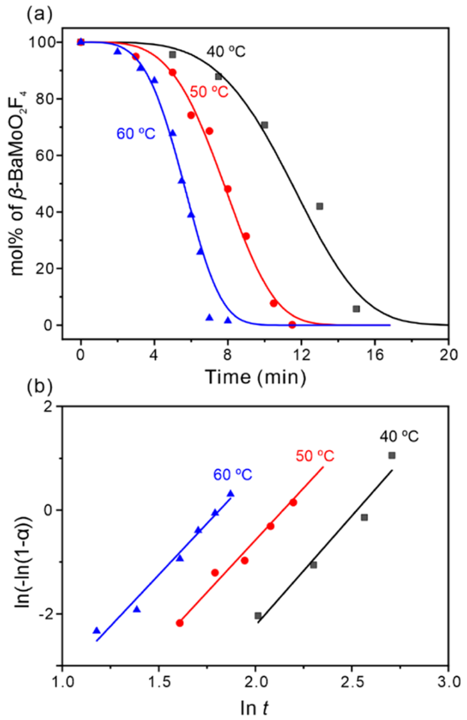

Figure 4. (a) Changes in mol % of β-BaMoO$_2$F$_4$ in the product during the transformation reactions and (b) Sharp−Hancock plots at different temperatures. The results were fitted by the Avrami equation.

To determine the origin of the enthalpy-driven stability of α-BaMoO$_2$F$_4$, densities of states (DOSs) for both compounds have also been thoroughly analyzed (Figure 6a). We found that O 2p orbitals mainly contribute to the valence band maximum (VBM) for α-BaMoO$_2$F$_4$, whereas F 2p orbitals contribute more to the VBM for β-BaMoO$_2$F$_4$. As discussed before, more F$^-$ anions interact with Ba^{2+} than O^{2-} anions do in α-BaMoO$_2$F$_4$. Considering that the HOMO of d^0 transition-

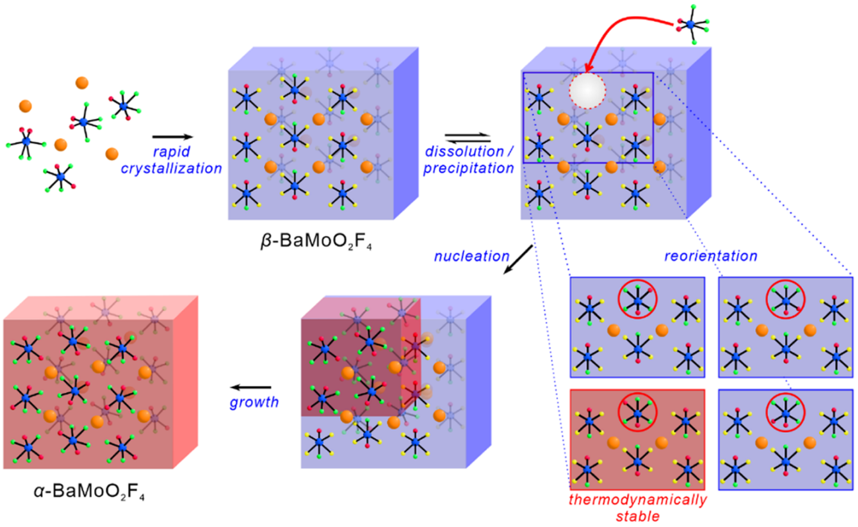

Figure 5. Proposed mechanism for the transformation of metastable β-BaMoO$_2$F$_4$ into thermodynamically stable α-BaMoO$_2$F$_4$. A rapid crystallization leads the MoO$_2$F$_4$ octahedra to locate in unstable positions and to crystallize in β-BaMoO$_2$F$_4$ with the O/F disorder. The reversible dissolution/precipitation reaction makes the MoO$_2$F$_4$ units find thermodynamically more stable positions and orientations. The newly formed fully ordered nuclei of α-BaMoO$_2$F$_4$ crystals grow over time.

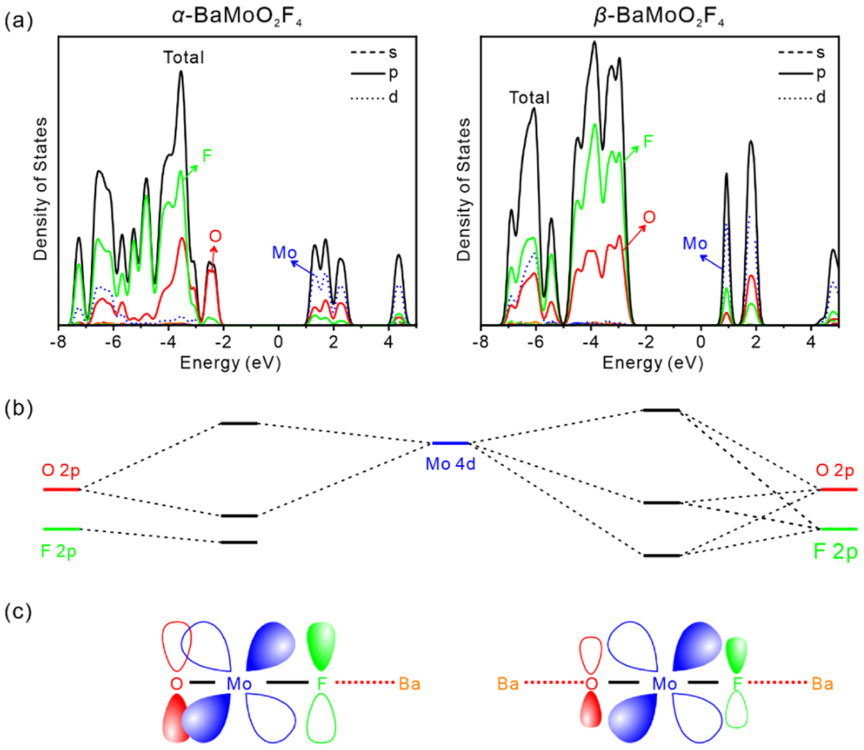

Figure 6. (a) Densities of states (DOSs), (b) molecular orbital (MO) diagrams, and (c) schematic π-interactions for α-BaMoO$_2$F$_4$ and β-BaMoO$_2$F$_4$. While O 2p orbitals mainly contribute to the valence band maximum (VBM) for α-BaMoO$_2$F$_4$, F 2p orbitals contribute more to the VBM for β-BaMoO$_2$F$_4$. More F$^-$ anions interact with Ba^{2+} than O^{2-} anions do in α-BaMoO$_2$F$_4$. Thus, π-interactions between Mo and O become stronger, while those between Mo and F become weaker in α-BaMoO$_2$F$_4$. The F$^-$ anions exhibiting weaker π-interactions with Mo are stabilized by interactions with Ba^{2+} cations in α-BaMoO$_2$F$_4$. In β-BaMoO$_2$F$_4$, π-interactions between Mo and O are rather disturbed because the existing O/F disorder forces O to interact with Ba.

metal cations in the octahedral coordination environment mainly consists of ligand 2p orbitals, the molecular orbital (MO) diagrams can be drawn as shown in Figure 6b. As the DOS and MO diagrams indicate, π-interactions between Mo and O become stronger, while those between Mo and F become weaker in α-BaMoO$_2$F$_4$. The F$^-$ anions exhibiting weaker π-interactions with Mo, however, are stabilized by interactions with Ba^{2+} cations. On the other hand, in β-BaMoO$_2$F$_4$, π-interactions between Mo and O are rather disturbed because the existing O/F disorder forces O to interact with Ba as well (Figure 6c). Therefore, the large enthalpy difference between α-BaMoO$_2$F$_4$ and β-BaMoO$_2$F$_4$ comes from the degree of Mo−O π-interactions that are strengthened with the help of Ba^{2+} cations. Also, the macroscopic polar NCS crystallization through the alignment of MoO_2F_4 octahedra might be the result of the optimized Ba–F interactions.

■ CONCLUSIONS

A series of NCS polar divalent metal molybdenum oxyfluorides, $AMoO_2F_4$ (A = Sr, Ba, and Pb), have been synthesized via hydrothermal reactions in high yields. The molecular compounds exhibit distorted CsCl-type structures consisting of A^{2+} cations and large distorted $MoO_2F_4^{2-}$ octahedra with a complete O/F ordering. A fast crystallization from the reaction between BaF_2 and MoO_3–HF solution at room temperature, however, results in a stoichiometrically equivalent metastable CS polymorph, β-$BaMoO_2F_4$, with the O/F disorder. IR spectra confirm that while α-$BaMoO_2F_4$ exhibits two distinct Mo–O and Mo–F vibrations at ca. 500–600 cm^{-1}, β-$BaMoO_2F_4$ with the O/F disorder exhibits a broad merged band in the region. The band gaps of the reported series compounds decrease as the polarizability of valence electrons in divalent cations increases. The title compounds with NCS structures show SHG efficiencies similar to that of α-SiO_2 because of the antiparallel alignment of the constituting distorted MoO_2F_4 octahedra. Crystals of $SrMoO_2F_4$ and α-$BaMoO_2F_4$ emit yellow and orange luminescence, respectively, upon irradiation with a UV lamp. A detailed kinetic study using PXRD indicates that β-$BaMoO_2F_4$ transforms into α-$BaMoO_2F_4$ three-dimensionally. The MoO_2F_4 octahedra located in unstable locations in the metastable β-$BaMoO_2F_4$ find thermodynamically more stable positions and orientations through the dissolution/precipitation process and form fully ordered α-$BaMoO_2F_4$ crystals. Calculations indicate that NCS α-$BaMoO_2F_4$ is an enthalpy-driven thermodynamically stable phase originating from the degree of Mo–O π-interactions influenced by Ba^{2+} cations. The study on a series of divalent metal molybdenum oxyfluorides provides new ways toward discovering novel functional metastable materials more systematically.

■ MATERIALS AND METHODS

Caution: The HF solution is highly corrosive! Proper protective equipment is essential for safety.

Materials. SrF_2 (Sigma-Aldrich, 99%), $BaCO_3$ (Daejung, 99.0%), BaF_2 (Kokusan, 98%), PbF_2 (Sigma-Aldrich, 99%), MoO_3 (Alfa Aesar, 99.5%), and HF (J. T. Baker, 48–51 wt % aq. solution) were used as received. $BaMoO_4$ was synthesized by a solid-state reaction. Stoichiometric amounts of $BaCO_3$ and MoO_3 were mixed and heated to 600 °C for 12 h.

Syntheses of $AMoO_2F_4$ (A = Sr, Ba, and Pb). Crystals of $SrMoO_2F_4$, α-$BaMoO_2F_4$, and $PbMoO_2F_4$ were grown by the hydrothermal method. First, 5 mmol (0.628 g) of SrF_2, 5 mmol (0.720 g) of MoO_3, and 0.8 mL of HF for $SrMoO_2F_4$; 1 mmol (0.297 g) of $BaMoO_4$ and 1 mL of HF for $BaMoO_2F_4$; and 1 mmol (0.245 g) of PbF_2, 10 mmol (1.439 g) of MoO_3, and 1.5 mL of HF for $PbMoO_2F_4$ were added into Teflon liners. Then, each Teflon liner was placed into the respective stainless steel autoclave. After sealing, the autoclaves were heated to 200 °C for 72 h and cooled to room temperature at a rate of 6 °C/h. The products were recovered by filtration and washed with acetone. Pure products of $SrMoO_2F_4$, α-$BaMoO_2F_4$, and $PbMoO_2F_4$ were obtained in 61.8, 61.9, and 84.2% yields, respectively, based on the corresponding metal fluoride (Figures S1–S3).

Syntheses of β-$BaMoO_2F_4$. A polycrystalline sample of β-$BaMoO_2F_4$ was synthesized at room temperature. First, 1 mmol of MoO_3 (0.144 g) was added into a Teflon liner containing 1 mL of 49% HF aqueous solution. Then, the liner was transferred to a stainless steel autoclave. After sealing, the autoclave was heated to 200 °C for 6 h and cooled to room temperature. A colorless MoO_3–HF solution was produced in the autoclave. Then, 1 mmol of BaF_2 was added into the MoO_3–HF solution, and the solution was stirred with a magnetic stirrer bar at 1000 rpm for 5 min. Polycrystalline β-$BaMoO_2F_4$ was obtained by filtration in 76.1% yield based on MoO_3.

■ ASSOCIATED CONTENT

Supporting Information

The Supporting Information is available free of charge at https://pubs.acs.org/doi/10.1021/acs.chemmater.1c00074.

Experimental details; experimental and calculated powder X-ray diffraction patterns; EDS analysis; IR spectra; UV–vis diffuse reflectance spectra; TGA diagrams; PL spectra; and band structures and densities of states (PDF)

X-ray crystallographic file for $AMoO_2F_4$ (A = Sr, Ba, and Pb) (CIF)

■ AUTHOR INFORMATION

Corresponding Author

Kang Min Ok – *Department of Chemistry, Sogang University, Seoul 04107, Korea;* orcid.org/0000-0002-7195-9089; Email: kmok@sogang.ac.kr

Authors

Hongil Jo – *Department of Chemistry, Sogang University, Seoul 04107, Korea;* orcid.org/0000-0002-0627-4921

Min Hyung Lee – *Department of Chemistry, University of Ulsan, Ulsan 44610, Korea;* orcid.org/0000-0003-2977-183X

Complete contact information is available at: https://pubs.acs.org/10.1021/acs.chemmater.1c00074

Notes

The authors declare no competing financial interest.

■ ACKNOWLEDGMENTS

This research was supported by the National Research Foundation of Korea (NRF) funded by the Ministry of Science and ICT (Grant nos. 2018R1A5A1025208 and 2019R1A2C3005530).

■ REFERENCES

(1) Norquist, A. J.; O'Hare, D. Kinetic and Mechanistic Investigations of Hydrothermal Transformations in Zinc Phosphates. *J. Am. Chem. Soc.* **2004**, *126*, 6673–6679.

(2) Perego, C.; Revel, R.; Durupthy, O.; Cassaignon, S.; Jolivet, J.-P. Thermal stability of TiO_2-anatase: Impact of nanoparticles morphology on kinetic phase transformation. *Solid State Sci.* **2010**, *12*, 989–995.

(3) Fernández-Carrión, A. J.; Escudero, A.; Suchomel, M. R.; Becerro, A. I. Structural and kinetic study of phase transitions in $LaYSi_2O_7$. *J. Eur. Ceram. Soc.* **2012**, *32*, 2477–2486.

(4) Ok, K. M.; Lee, D. W.; Smith, R. I.; O'Hare, D. Time-Resolved in Situ Neutron Diffraction under Supercritical Hydrothermal Conditions: A Study of the Synthesis of $KTiOPO_4$. *J. Am. Chem. Soc.* **2012**, *134*, 17889–17891.

(5) Zhou, S.; Wei, Y.; Li, B.; Ma, B.; Wang, C.; Wang, H. Kinetics study on the dehydroxylation and phase transformation of $Mg_3Si_2O_5(OH)_4$. *J. Alloys Compd.* **2017**, *713*, 180–186.

(6) Cheetham, A. K.; Kieslich, G.; Yeung, H. H. M. Thermodynamic and Kinetic Effects in the Crystallization of Metal–Organic Frameworks. *Acc. Chem. Res.* **2018**, *51*, 659–667.

(7) Oh, S.-J.; Lim, S.-J.; You, T.-S.; Ok, K. M. From a Metastable Layer to a Stable Ring: A Kinetic Study for Transformation Reactions of $Li_2Mo_3TeO_{12}$ to Polyoxometalates. *Chem. - Eur. J.* **2018**, *24*, 6712−6716.

(8) Henkelis, S. E.; Mazur, M.; Rice, C. M.; Wheatley, P. S.; Ashbrook, S. E.; Morris, R. E. Kinetics and Mechanism of the Hydrolysis and Rearrangement Processes within the Assembly−Disassembly−Organization−Reassembly Synthesis of Zeolites. *J. Am. Chem. Soc.* **2019**, *141*, 4453−4459.

(9) Zhao, J.; Brugger, J.; Pring, A. Mechanism and kinetics of hydrothermal replacement of magnetite by hematite. *Geosci. Front.* **2019**, *10*, 29−41.

(10) Yu, J.; Ruengkajorn, K.; Crivoi, D.-G.; Chen, C.; Buffet, J.-C.; O'Hare, D. High gas barrier coating using non-toxic nanosheet dispersions for flexible food packaging film. *Nat. Commun.* **2019**, *10*, No. 2398.

(11) Broge, N. L. N.; Bondesgaard, M.; Søndergaard-Pedersen, F.; Roelsgaard, M.; Iversen, B. B. Autocatalytic Formation of High-Entropy Alloy Nanoparticles. *Angew. Chem., Int. Ed.* **2020**, *59*, 21920−21924.

(12) Kodani, S.; Koga, N. Kinetics of contracting geometry-type reactions in the solid state: implications from the thermally induced transformation processes of α-oxalic acid dihydrate. *Phys. Chem. Chem. Phys.* **2020**, *22*, 19560−19572.

(13) Kageyama, H.; Hayashi, K.; Maeda, K.; Attfield, J. P.; Hiroi, Z.; Rondinelli, J. M.; Poeppelmeier, K. R. Expanding frontiers in materials chemistry and physics with multiple anions. *Nat. Commun.* **2018**, *9*, No. 772.

(14) Wissel, K.; Malik, A. M.; Vasala, S.; Plana-Ruiz, S.; Kolb, U.; Slater, P. R.; da Silva, I.; Alff, L.; Rohrer, J.; Clemens, O. Topochemical Reduction of $La_2NiO_3F_2$: The First Ni-Based Ruddlesden−Popper n = 1 T′-Type Structure and the Impact of Reduction on Magnetic Ordering. *Chem. Mater.* **2020**, *32*, 3160−3179.

(15) Cai, E.; Zheng, Y.; Wang, S. Modifying optical and photochemical properties of bismuth oxyfluoride $BiTe_3O_7F$ via stoichiometry alteration between Bi^{3+} and Te^{4+} ions. *J. Alloys Compd.* **2020**, *847*, No. 156465.

(16) Chen, J.; Hu, C.-L.; Zhang, X.-H.; Li, B.-X.; Yang, B.-P.; Mao, J.-G. $CsVO_2F(IO_3)$: An Excellent SHG Material Featuring an Unprecedented 3D $[VO_2F(IO_3)]^-$ Anionic Framework. *Angew. Chem., Int. Ed.* **2020**, *59*, 5381−5384.

(17) Hu, W.; Shan, P.; Sun, T.; Liu, H.; Zhang, J.; Liu, X.; Kong, Y.; Xu, J. Preparation, nonlinear optical properties, and theoretical analysis of the non-centrosymmetric bismuth oxyfluoride, $Bi_7F_{11}O_5$. *J. Alloys Compd.* **2016**, *658*, 788−794.

(18) Zhang, M.; Su, X.; Mutailipu, M.; Yang, Z.; Pan, S. $Bi_3OF_3(IO_3)_4$: Metal Oxyiodate Fluoride Featuring a Carbon-Nanotube-like Topological Structure with Large Second Harmonic Generation Response. *Chem. Mater.* **2017**, *29*, 945−949.

(19) Luo, M.; Liang, F.; Song, Y.; Zhao, D.; Ye, N.; Lin, Z. Rational Design of the First Lead/Tin Fluorooxoborates $MB_2O_3F_2$ (M = Pb, Sn), Containing Flexible Two-Dimensional $[B_6O_{12}F_6]_\infty$ Single Layers with Widely Divergent Second Harmonic Generation Effects. *J. Am. Chem. Soc.* **2018**, *140*, 6814−6817.

(20) Cho, E. J.; Oh, S.-J.; Jo, H.; Lee, J.; You, T.-S.; Ok, K. M. Layered Bismuth Oxyfluoride Nitrates Revealing Large Second-Harmonic Generation and Photocatalytic Properties. *Inorg. Chem.* **2019**, *58*, 2183−2190.

(21) Chung, J. Y.; Jo, H.; Yeon, S.; Byun, H. R.; You, T.-S.; Jang, J. I.; Ok, K. M. $Bi_3(SeO_3)_3(Se_2O_5)F$: A Polar Bismuth Selenite Fluoride with Polyhedra of Highly Distortive Lone Pair Cations and Strong Second-Harmonic Generation Response. *Chem. Mater.* **2020**, *32*, 7318−7326.

(22) Mutailipu, M.; Pan, S. Emergent Deep-Ultraviolet Nonlinear Optical Candidates. *Angew. Chem., Int. Ed.* **2020**, *59*, 20302−20317.

(23) Zhou, J.; Wu, H.; Yu, H.; Jiang, S.; Hu, Z.; Wang, J.; Wu, Y.; Halasyamani, P. S. $BaF_2TeF_2(OH)_2$: A UV Nonlinear Optical Fluorotellurite Material Designed by Band-Gap Engineering. *J. Am. Chem. Soc.* **2020**, *142*, 4616−4620.

(24) Deng, Y.; Huang, L.; Dong, X.; Wang, L.; Ok, K. M.; Zeng, H.; Lin, Z.; Zou, G. $K_2Sb(P_2O_7)F$: Cairo Pentagonal Layer with Bifunctional Genes Reveal Optical Performance. *Angew. Chem., Int. Ed.* **2020**, *59*, 21151−21156.

(25) Lee, H.; Ok, K. M. $Na_2Mg_{1-x}Zn_xSiO_4$ ($0 \leq x \leq 1$): Noncentrosymmetric Sodium Metal Silicate Solid Solutions with Ultraviolet Nonlinear Optical Properties. *Bull. Korean Chem. Soc.* **2020**, *41*, 139−142.

(26) Mutailipu, M.; Poeppelmeier, K. R.; Pan, S. Borates: A Rich Source for Optical Materials. *Chem. Rev.* **2021**, *121*, 1130−1202.

(27) Luo, M.; Liang, F.; Hao, X.; Lin, D.; Li, B.; Lin, Z.; Ye, N. Rational Design of the Nonlinear Optical Response in a Tin Iodate Fluoride $Sn(IO_3)_2F_2$. *Chem. Mater.* **2020**, *32*, 2615−2620.

(28) Ok, K. M.; Halasyamani, P. S.; Casanova, D.; Llunell, M.; Alemany, P.; Alvarez, S. Distortions in Octahedrally Coordinated d^0 Transition Metal Oxides: A Continuous Symmetry Measures Approach. *Chem. Mater.* **2006**, *18*, 3176−3183.

(29) Hwang, J. Y.; Ok, K. M. A Plausible Formation Mechanism of Polyoxoperoxomolybdates With Variable Structures. *Bull. Korean Chem. Soc.* **2020**, *41*, 588−591.

(30) Huang, J.; Guo, S.; Zhang, Z.; Yang, Z.; Pan, S. Designing excellent mid-infrared nonlinear optical materials with fluorooxo-functional group of d^0 transition metal oxyfluorides. *Sci. China Mater.* **2019**, *62*, 1798−1806.

(31) Liang, M.-L.; Ma, Y.-X.; Hu, C.-L.; Kong, F.; Mao, J.-G. $Ba(MoO_2F)_2(QO_3)_2$ (Q = Se, Te): Partial Fluorination of MoO_6 Octahedra Enabling Two Polar Solids with Strong and Phase Matchable SHG Response. *Chem. Mater.* **2020**, *32*, 9688−9695.

(32) Hancock, J. C.; Nisbet, M. L.; Zhang, W.; Halasyamani, P. S.; Poeppelmeier, K. R. Periodic Tendril Perversion and Helices in the $AMoO_2F_3$ (A = K, Rb, NH_4, Tl) Family. *J. Am. Chem. Soc.* **2020**, *142*, 6375−6380.

(33) Ishikawa, H.; Munaò, I.; Bode, B. E.; Hiroi, Z.; Lightfoot, P. $Na_2MoO_{2-\delta}F_{4+\delta}$ − a perovskite with a unique combination of atomic orderings and octahedral tilts. *Chem. Commun.* **2015**, *51*, 15469−15471.

(34) Fry, A. M.; Woodward, P. M. Structures of α-$K_3MoO_3F_3$ and α-$Rb_3MoO_3F_3$: Ferroelectricity from Anion Ordering and Noncooperative Octahedral Tilting. *Cryst. Growth Des.* **2013**, *13*, 5404−5410.

(35) He, S.; Xu, F.; Han, T.; Lu, Z.; Wang, W.; Peng, J.; Du, F.; Yang, F.; Ye, X. A Mn^{4+}-doped oxyfluoride phosphor with remarkable negative thermal quenching and high color stability for warm WLEDs. *Chem. Eng. J.* **2020**, *392*, No. 123657.

(36) Stoll, C.; Seibald, M.; Baumann, D.; Huppertz, H. HF-Free Solid-State Synthesis of the Oxyfluoride Phosphor $K_3MoOF_7{:}Mn^{4+}$. *Eur. J. Inorg. Chem.* **2019**, *2019*, 3383−3388.

(37) Liu, Y.; Li, H.; Tang, S.; Zhou, Q.; Wang, K.; Tang, H.; Wang, Z. A red-emitting phosphor $K_2[MoO_2F_4]\bullet H_2O{:}Mn^{4+}$ for warm white light-emitting diodes with a high color rendering index. *Mater. Res. Bull.* **2020**, *122*, No. 110675.

(38) Reshak, A. H. Revealing the electronic structure and optical properties of $K_6[Mo_4O_8F_{10}]$ novel molybdenum oxyfluoride materials. *Philos. Mag.* **2016**, *96*, 3131−3142.

(39) Shi, T.; Zhang, F.; Li, Y.; Gao, L.; Yang, Z.; Pan, S. Structural Diversity of Molybdate Iodate and Fluoromolybdate: Syntheses, Structures, and Calculations on $Na_3(MoO_4)(IO_3)$ and $Na_3Cs(MoO_2F_4)_2$. *Inorg. Chem.* **2020**, *59*, 3034−3041.

(40) Brese, N. E.; Okeeffe, M. Bond-Valence Parameters for Solids. *Acta Crystallogr., Sect. B: Struct. Sci.* **1991**, *47*, 192−197.

(41) Socrates, G. *Infrared and Raman Characteristic Group Frequencies: Tables and Charts*; Wiley: West Sussex, 2001; pp 323−327.

(42) Liang, M.-L.; Ma, Y.-X.; Hu, C.-L.; Kong, F.; Mao, J.-G. $A(VO_2F)(SeO_3)$ (A = Sr, Ba) and $Ba(MOF_2)(TeO_4)$ (M = Mo, W): first examples of alkali-earth selenites/tellurites with a fluorinated d^0-TM octahedron. *Dalton Trans.* **2018**, *47*, 1513−1519.

(43) Jo, H.; Ok, K. M. Histidinium-Driven Chirality Control of Self-Assembled Hybrid Molybdenum Oxyfluorides. *Chem. - Eur. J.* **2019**, *25*, 15871−15878.

(44) Kubelka, P.; Munk, F. Z. Ein Beitrag Zur Optik Der Farbanstriche. *Z. Tech. Phys.* **1931**, *12*, 593−601.

(45) Zhang, X.; Nie, J.; Liu, S.; Li, Y.; Qiu, J. Deep-red photoluminescence and long persistent luminescence in double perovstkite-type La_2MgGeO_6:Mn^{4+}. *J. Am. Ceram. Soc.* **2018**, *101*, 1576−1584.

(46) Wu, M.; Chen, W.; Zhang, Y.; Zhang, J.; Chen, G.; Zheng, Z. Defects enhanced photoluminescence of Mn^{2+}-doped ZrP_2O_7 blue LLP materials. *J. Alloys Compd.* **2019**, *789*, 375−380.

(47) Cai, P.; Qin, L.; Chen, C.; Wang, J.; Seo, H. J. Luminescence, energy transfer and optical thermometry of a novel narrow red emitting phosphor: $Cs_2WO_2F_4$:Mn^{4+}. *Dalton Trans.* **2017**, *46*, 14331−14340.

(48) Ayer, G. B.; Klepov, V. V.; Smith, M. D.; Hu, M.; Yang, Z.; Martin, C. R.; Morrison, G.; zur Loye, H.-C. $BaWO_2F_4$: a mixed anion X-ray scintillator with excellent photoluminescence quantum efficiency. *Dalton Trans.* **2020**, *49*, 10734−10739.

(49) Huhn, W. P.; Blum, V. One-hundred-three compound band-structure benchmark of post-self-consistent spin-orbit coupling treatments in density functional theory. *Phys. Rev. Mater.* **2017**, *1*, No. 033803.

(50) Goyal, A.; McKechnie, S.; Pashov, D.; Tumas, W.; van Schilfgaarde, M.; Stevanović, V. Origin of Pronounced Nonlinear Band Gap Behavior in Lead−Tin Hybrid Perovskite Alloys. *Chem. Mater.* **2018**, *30*, 3920−3928.

(51) Lai, K.; Yan, C.-L.; Gao, L.-Q.; Zhang, W.-B. AI_3 (A = As, Sb) Single Layers and Their vdW Heterostructure for Photocatalysis and Solar Cell Applications. *J. Phys. Chem. C* **2018**, *122*, 7656−7663.

(52) Ming, H.; Zhang, J.; Liu, L.; Peng, J.; Du, F.; Ye, X.; Yang, Y.; Nie, H. A novel Cs_2NbOF_5:Mn^{4+} oxyfluoride red phosphor for light-emitting diode devices. *Dalton Trans.* **2018**, *47*, 16048−16056.

(53) Wang, Z.; Yang, Z.; Yang, Z.; Wei, Q.; Zhou, Q.; Ma, L.; Wang, X. Red Phosphor Rb_2NbOF_5:Mn^{4+} for Warm White Light-Emitting Diodes with a High Color-Rendering Index. *Inorg. Chem.* **2019**, *58*, 456−461.

(54) Avrami, M. Kinetics of Phase Change. I General Theory. *J. Chem. Phys.* **1939**, *7*, 1103−1112.

(55) Avrami, M. Kinetics of Phase Change. II Transformation-Time Relations for Random Distribution of Nuclei. *J. Chem. Phys.* **1940**, *8*, 212−224.

(56) Eyring, H. The Activated Complex in Chemical Reactions. *J. Chem. Phys.* **1935**, *3*, 107−115.

(57) Chevrier, V. L.; Hautier, G.; Ong, S. P.; Doe, R. E.; Ceder, G. First-principles study of iron oxyfluorides and lithiation of FeOF. *Phys. Rev. B* **2013**, *87*, No. 094118.

(58) Krylov, A. S.; Sofronova, S. N.; Kolesnikova, E. M.; Ivanov, Y. N.; Sukhovsky, A. A.; Goryainov, S. V.; Ivanenko, A. A.; Shestakov, N. P.; Kocharova, A. G.; Vtyurin, A. N. Experimental and theoretical methods to study structural phase transition mechanisms in $K_3WO_3F_3$ oxyfluoride. *J. Solid State Chem.* **2014**, *218*, 32−37.

(59) Manzoor, A.; Pandey, S.; Chakraborty, D.; Phillpot, S. R.; Aidhy, D. S. Entropy contributions to phase stability in binary random solid solutions. *npj Comput. Mater.* **2018**, *4*, No. 47.

(60) Heier, K. R.; Norquist, A. J.; Wilson, C. G.; Stern, C. L.; Poeppelmeier, K. R. $[pyH]_2[Cu(py)_4(MX_6)_2]$ (MX_6 = $ZrF_6{}^{2-}$, $NbOF_5{}^{2-}$, $MoO_2F_4{}^{2-}$; py = Pyridine): Rarely Observed Ordering of Metal Oxide Fluoride Anions. *Inorg. Chem.* **1998**, *37*, 76−80.

(61) Gautier, R.; Gautier, R.; Chang, K. B.; Poeppelmeier, K. R. On the Origin of the Differences in Structure Directing Properties of Polar Metal Oxyfluoride $[MO_xF_{6-x}]^{2-}$ (x = 1, 2) Building Units. *Inorg. Chem.* **2015**, *54*, 1712−1719.

(62) Maggard, P. A.; Kopf, A. L.; Stern, C. L.; Poeppelmeier, K. R.; Ok, K. M.; Halasyamani, P. S. From Linear Inorganic Chains to Helices: Chirality in the $M(pyz)(H_2O)_2MoO_2F_4$ (M = Zn, Cd) Compounds. *Inorg. Chem.* **2002**, *41*, 4852−4858.

(63) Sergienko, V. S.; Porai Koshits, M. A.; Shodatchova, T. S. Crystal Structure of $Rb_2MoO_2F_4$. *Zh. Strukt. Khim.* **1972**, *13*, 461−467.

(64) Udovenko, A. A.; Vasiliev, A. D.; Laptash, N. M. Orientational disorder and phase transitions in crystals of dioxofluoromolybdate, $(NH_4)_2MoO_2F_4$. *Acta Crystallogr., Sect. B: Struct. Sci.* **2010**, *66*, 34−39.

(65) Marvel, M. R.; Pinlac, R. A. F.; Lesage, J.; Stern, C. L.; Poeppelmeier, K. R. Chemical Hardness and the Adaptive Coordination Behavior of the d0 Transition Metal Oxide Fluoride Anions. *Z. Anorg. Allg. Chem.* **2009**, *635*, 869−877.